optica

Optomechanically amplified wavelength conversion in diamond microcavities: supplementary material

MATTHEW MITCHELL, DAVID P. LAKE, AND PAUL E. BARCLAY[*]

Department of Physics and Astronomy and Institute for Quantum Science and Technology, University of Calgary, Calgary, AB, T2N 1N4, Canada

[*]*Corresponding author: pbarclay@ucalgary.ca*

This document provides supplementary information to "Optomechanically amplified wavelength conversion in diamond microcavities," https://doi.org/10.1364/OPTICA.6.000832. First, the model for fitting both optomechanically induced transparency spectra measured via phase and amplitude electro–optic modulatos is given. Second, an example of wavelength down–conversion and up–conversion in a second diamond microdisk, and a correction in fitting the optomechanically induced transparency window for a doublet mode is described. Third, the calibration of the vacuum optomechanical coupling rate, g_0, is briefly described. Finally an estimation of the amplified wavelength conversion gain is presented.

1. ELECTRO–OPTIC MODULATION MODEL

When modelling the predicted output spectra of the optomechanical cavities studied in this work the details of how the probe fields are generated are vital, due to the sensitivity of the cavity to both phase and amplitude fluctuations. A variety of constructions exist for implementing an optical phase or amplitude modulator. The LiNbO$_3$ electro–optic modulators (EOM) utilized in this work were purchased from EOSpace where the amplitude modulator used is Z–cut (pre–chirp) with an alpha chirp parameter of $\alpha_{\mathrm{chirp}} \sim 0.6 - 0.8$. In practice this results in both amplitude and phase modulation which must be taken into account when considering the optical transmission and reflection by the optical cavity.

A phasor picture can prove useful when visualizing the differences between pure phase and amplitude modulation as illustrated in the attached animations (Supplement 2 & 3), where inspiration was taken from Ref. [1]. Here a frame rotating with the carrier frequency is used such that the electric field vector appears stationary. We observe from this animation that for pure phase modulation the generated sidebands are out of phase when re–phasing in the real plane leading to no amplitude modulation, while for the pure amplitude modulation case they are π out of phase when re–phasing in the real plane. In practice our amplitude modulator does not provide pure amplitude modulation. To account for this, we allow the phase of the carrier to

be a variable dependent on the type of EOM used to develop a model capable of describing an EOM operating between the pure amplitude and phase modulation regime. First we describe optical field amplitude generated by the EOM and then input to the cavity α_{in} as:

$$\alpha_{\mathrm{in}} = \alpha \left(e^{i\phi} + \frac{\beta}{2} e^{i\omega t} + \frac{\beta}{2} e^{-i\omega t} \right), \tag{S1}$$

where α is the carrier optical field amplitude, β is the modulation index, and ω is the modulation frequency. When $\phi = 0 \pm n\pi$ the field for a pure amplitude modulator is described and for $\phi = \pi/2 \pm n\pi$ a pure phase modulator. To use this model to predict the observed cavity output spectra in this work we begin by writing the input optical field frequency components as $\alpha_{\mathrm{in}}^0 = \alpha e^{i\phi}$, $\alpha_{\mathrm{in}}^+ = \frac{\alpha\beta}{2} e^{-i\omega t}$, and $\alpha_{\mathrm{in}}^- = \frac{\alpha\beta}{2} e^{i\omega t}$. Then the cavity transmission and reflection amplitudes are given by:

$$t_{\mathrm{out}} = t_{\mathrm{out}}^+ + t_{\mathrm{out}}^0 + t_{\mathrm{out}}^- \tag{S2}$$

and

$$r_{\mathrm{out}} = r_{\mathrm{out}}^+ + r_{\mathrm{out}}^0 + r_{\mathrm{out}}^- \tag{S3}$$
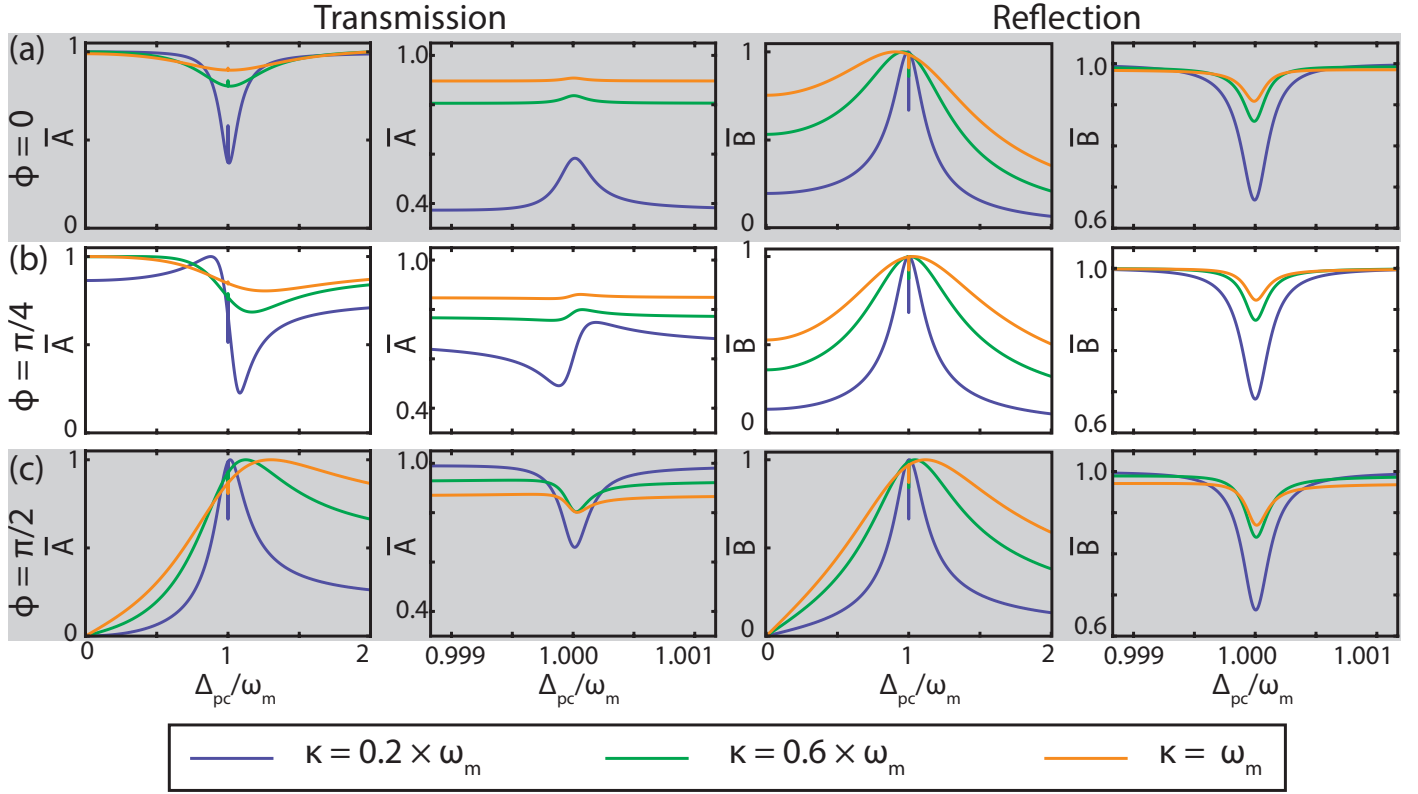
where

Fig. S1. Model for reflection and transmission spectra as a function of probe field detuning, Δ_{pc} and sideband phase parameter ϕ for a red–detuned control field with $\Delta_{oc} = \omega_m$, $Q_m = 5000$, $G = 4.78$ MHz, $\kappa_e = 0.25 \cdot \kappa$, and varying sideband resolution shown in the legend.

$$t_{out}^+ = t^+ \alpha_{in}^+ \qquad \text{(S4)}$$
$$t_{out}^0 = t^0 \alpha_{in}^0$$
$$t_{out}^- = t^- \alpha_{in}^-$$

and

$$r_{out}^+ = r^+ \alpha_{in}^+ \qquad \text{(S5)}$$
$$r_{out}^0 = r^0 \alpha_{in}^0$$
$$r_{out}^- = r^- \alpha_{in}^-.$$

Here the terms (t^+, t^0, t^-) and (r^+, r^0, r^-) describe the cavity transmission or reflection amplitude, respectively, as seen by each frequency component of the input field, defined as follows. We now consider the power measured by the photodetector in transmission and reflection, $|t_{out}|^2 = t_{out}^* t_{out}$, and $|r_{out}|^2 = r_{out}^* r_{out}$:

$$|t_{out}|^2 = |t^0|^2|\alpha_{in}^0|^2 + t^{0*}t^+\alpha_{in}^{0*}\alpha_{in}^+ + t^0 t^{-*}\alpha_{in}^0\alpha_{in}^{-*} + c.c \qquad \text{(S6)}$$

and

$$|r_{out}|^2 = |r^0|^2|\alpha_{in}^0|^2 + r^{0*}r^+\alpha_{in}^{0*}\alpha_{in}^+ + r^0 r^{-*}\alpha_{in}^0\alpha_{in}^{-*} + c.c, \qquad \text{(S7)}$$

where we have neglected terms that are of $\mathcal{O}(\beta^2)$. Substituting our expressions for the input fields gives:

$$|t_{out}|^2 = |t^0|^2\alpha^2 + \alpha^2\frac{\beta}{2}[t^{0*}t^+ e^{-i\phi} + t^0 t^{-*}e^{i\phi}]e^{-i\omega t}$$
$$+ \alpha^2\frac{\beta}{2}[t^0 t^{+*}e^{i\phi} + t^{0*}t^- e^{-i\phi}]e^{i\omega t} \qquad \text{(S8)}$$

and

$$|r_{out}|^2 = |r^0|^2\alpha^2 + \alpha^2\frac{\beta}{2}[r^{0*}r^+ e^{-i\phi} + r^0 r^{-*}e^{i\phi}]e^{-i\omega t}$$
$$+ \alpha^2\frac{\beta}{2}[r^0 r^{+*}e^{i\phi} + r^{0*}r^- e^{-i\phi}]e^{i\omega t}. \qquad \text{(S9)}$$

In general the above may be written as

$$|t_{out}|^2 = |t^0|^2\alpha^2 + \alpha^2\beta|A|\cos(\omega t - \arg\{A\}) \qquad \text{(S10)}$$

and

$$|r_{out}|^2 = |r^0|^2\alpha^2 + \alpha^2\beta|B|\cos(\omega t - \arg\{B\}), \qquad \text{(S11)}$$

where

$$A = (t^{0*}t^+ e^{-i\phi} + t^0 t^{-*}e^{i\phi}) \qquad \text{(S12)}$$

and

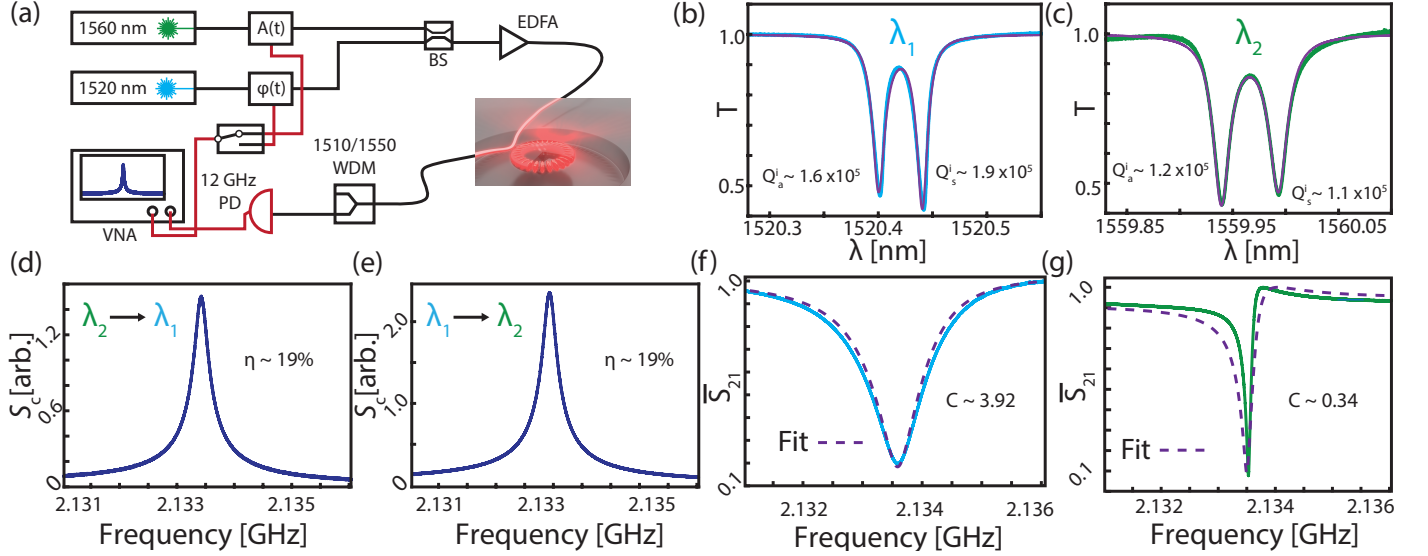$$B = (r^{0*}r^+ e^{-i\phi} + r^0 r^{-*}e^{i\phi}). \qquad \text{(S13)}$$

Fig. S2. (a) Experimental setup used for frequency up– and down–conversion. Phase and amplitude EOM's driven by the vector network analyzer (VNA) are used to generate the probe fields from the control fields where an RF switch controls which laser to modulate. A 50%/50% waveguide coupler combines the input fields which are coupled to the microdisk via a dimpled tapered fiber. A 1510/1550 WDM is used to filter the output of the cavity and the photodetected signal is analyzed by the VNA. (b,c) Optical whispering gallery mode resonances used in frequency conversion process. Intrinsic optical quality factors for the symmetric and anti–symmetric doublet modes labelled. (d,e) Beat note between converted photons and control field of the same color measured on the VNA for frequency up– and down– conversion respectively. (f,g) OMIT spectra for the λ_1 and λ_2 optical modes, respectively, where the cooperativity is extracted from fitting the OMIT lineshape.

The measured vector network analyzer (VNA) signal for the phase and amplitude quadrature are modeled by $\arg\{A\}$ ($\arg\{B\}$) and $|A|$ ($|B|$), respectively, for transmission (reflection) by the cavity. Additionally, by selecting the proper value of ϕ the response for a phase EOM, amplitude EOM, or mixture of both may be modelled. The bare cavity transmission amplitude $t^0(\Delta_{\mathrm{oc}})$ is given by:

$$t^0(\Delta_{\mathrm{oc}}) = 1 - \frac{\kappa_e/2}{i(\Delta_{\mathrm{oc}}) + \kappa/2} \tag{S14}$$

and for a red–detuned control field, the sideband transmission amplitudes as a function of Δ_{pc} are given by:

$$t^{\pm}(\pm\Delta_{\mathrm{pc}}) = 1 - \frac{\kappa_e/2}{i(\Delta_{\mathrm{oc}} - (\pm\Delta_{\mathrm{pc}})) + \kappa/2 + \frac{Ng_0^2}{i(\omega_m - (\pm\Delta_{\mathrm{pc}})) + \Gamma_m/2}}. \tag{S15}$$

In the main text the reflected amplitude measured on the VNA is fit to $|B|$ by taking $r = 1 - t$, and substituting Eqns. S14 and S15 into Eqn. S13, and choosing the appropriate value of ϕ depending on the EOM used. In order to determine ϕ for the amplitude EOM used in this work the phase difference (2θ) between the sidebands was determined from the chirp parameter, α_{chirp}, as:

$$\tan\theta \approx \alpha_{\mathrm{chirp}}\cot\left(\frac{\varphi}{2}\right) \tag{S16}$$

assuming a small–modulation amplitude ($\beta \ll 1$), where φ is the constant phase delay between the two interferometer arms, and $\varphi = \pi/2$ when biased at quadrature [2]. Through fitting the OMIT spectra obtained with the amplitude EOM in both the main text and in the following section, $\alpha_{\mathrm{chirp}} \sim 0.70$ was found to provide the best fit; this value is within the bounds provided by the manufacturer.

For reference, the behavior of the model described above is shown in Fig. S1 for various ϕ and degree to which the system is sideband resolved. In particular it can be seen that for a non–pure amplitude modulator the observed VNA transmission spectra, $\bar{A} = |A|/\max(|A|)$ can a resemble that of the reflection spectra, $\bar{B} = |B|/\max(|B|)$.

2. WAVELENGTH UP– AND DOWN–CONVERSION

For completeness, a demonstration of wavelength up– and down– conversion in the same device is presented here with an alternative microdisk on the same single–crystal diamond substrate as presented in the main text. This device exhibited two high-Q optical modes that were within the operating range of a 1510/1550 nm wavelength division multiplexer (Montclair MFT-MC-51) which allowed the filtering of each mode from the fiber taper transmission, which we were unable to do with the device studied in the main text. Contrary to the measurement presented in the main text this device was measured in transmission instead of reflection, as outlined in Fig. S2(a). Here two optical modes at $\lambda_1 = 1520$ nm and $\lambda_2 = 1560$ nm, as shown in Fig. S2(b,c), were coupled to the fundamental radial breathing mode (RBM) at $\omega_m/2\pi = 2.135$ GHz, with $Q_m \sim 7,500$, for a similarly sized microdisk as studied in the main text. The measurement of both the up– and down–converted signal with the vector network analyzer is shown in Fig. S2(d,e).

During this measurement symmetric or red mode of the λ_1 doublet was used such that the blue sideband of the EOM was off-resonance. However, the anti–symmetric or blue mode of the λ_2 doublet was used in the conversion process due it's the higher optical–Q. When setting up the experiment, balancing C for each mode was performed by maximizing the contrast of each OMIT window, while attempting to reach $C_1 = C_2 > 1$. However, the relatively small splitting of this doublet led to a modification

to the OMIT window spectral profile, due to participation of the red mode of the doublet, resulting in lower C than expected based on the depth of the OMIT feature alone, and an overall low conversion efficiency due to the mismatch of C_1 and C_2. To account for this contribution the transmission amplitude for the blue sideband, $t^-(-\Delta_{\text{pc}})$, for an optical doublet was included as

$$t^-(-\Delta_{\text{pc}}) = 1 - \sqrt{\kappa_e/2}(a_s(-\Delta_{\text{pc}}) + a_a(-\Delta_{\text{pc}})), \quad \textbf{(S17)}$$

where

$$a_{s,a}(-\Delta_{\text{pc}}) = \frac{-\sqrt{\kappa_e/2}}{-\kappa_{s,a}/2 + i((\Delta_{\text{oc}} - (-\Delta_{\text{pc}})) \pm \kappa_{bs}/2)} \quad \textbf{(S18)}$$

are the symmetric (a_s) and anti-symmetric (a_a) combinations of the degenerate clockwise and counter–clockwise propagating travelling wave modes of the microdisk [3]. Here κ_{bs} is the backscattering rate between each mode, and κ_e is taken to be equal for each doublet.

The OMIT spectrum obtained with the phase EOM shown in Fig. S2(f) was fit by including both side bands ($t^\pm(\pm\Delta_{\text{pc}})$) where a small phase delay ($< 5°$) in sidebands was included to obtain good agreement with the spectra. In order to fit the OMIT spectrum obtained with the amplitude EOM shown in Fig. S2(g) both the inclusion of the chirp induced sideband phase difference ($2\theta \sim 70°$) and the doublet transmission profile for ($t^-(-\Delta_{\text{pc}})$ were included. While the quality of this fit is inferior compared to the other OMIT fits, the inclusion of the doublet transmission profile reproduces the sharp, large contrast OMIT feature that in reality has $C < 1$. This results in $C_1 \sim 3.92$, $C_2 \sim 0.34$, and $\eta_{\text{int}} \sim 15\%$, for $\eta_{1,2} \sim 19\%$, resulting in $\eta_{\text{ext}} = 0.55\%$ for the device studied here. The fiber taper input power, P_{in}, was ~ 17 mW and ~ 4.2 mW, respectively, corresponding to $N_1 \sim 7.0 \times 10^5$ and $N_2 \sim 9.0 \times 10^4$ for λ_1 and λ_2. Through the use of an additional EDFA it should be possible to reach $C_1 = C_2 > 1$, through independent control of N for each mode; assuming that both modes could reach $C \sim 2$ would give $\eta_{\text{int}} \sim 64\%$.

3. OPTOMECHANICAL COUPLING CALIBRATION

To estimate the vacuum optomechanical coupling rate of the λ_1 and λ_2 optical modes studied in the main text to the fundamental RBM the frequency noise method developed by Gorodetksy et al., which is now widely used in cavity optomechanics [4–6] was utilized. Here we compare the power spectral densities resulting from the thermomechanical cavity frequency fluctuations and a calibration tone generated with a phase modulator (EOSpace). By placing the frequency of the calibration tone, ω_{cal}, close to the mechanical frequency, ω_m, the transduction coefficients can be approximated as being equal, and g_0 can be calculated as

$$g_0 = \frac{\beta\omega_{\text{cal}}}{2}\sqrt{\frac{1}{n_{\text{th}}}\frac{S_{\text{mech}}(\omega_m)}{S_{\text{cal}}(\omega_{\text{cal}})}}. \quad \textbf{(S19)}$$

Here $\beta = (V_p/V_\pi)\pi$ is the modulation index of the phase modulator, where V_p is the amplitude of the driving RF signal, and V_π is the modulators half wave voltage; $n_{\text{th}} = k_B T/\hbar\omega_m$ is the thermal occupation of the mechanical mode, and $S_{\text{cal}}(\omega_{\text{cal}}), S_{\text{mech}}(\omega_{\text{mech}})$ are the integrated powers in the calibration tone and mechanical mode response, obtained from the power spectral density measured on the real time spectrum analyzer in Fig. S3.
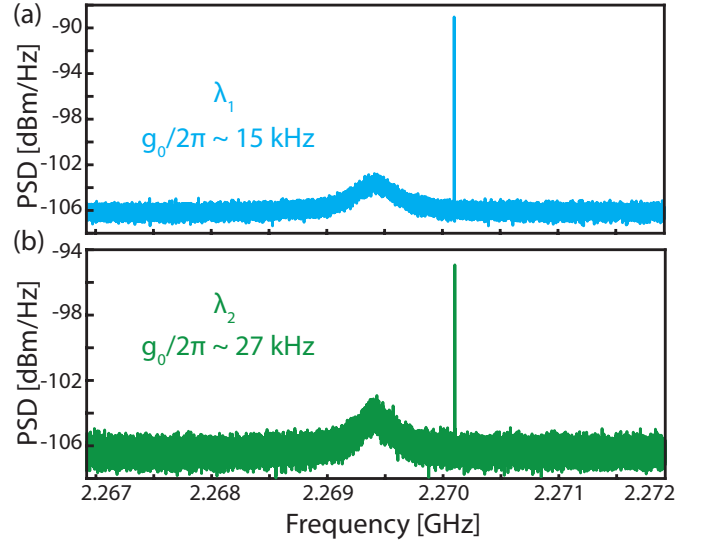

Fig. S3. Phase tone calibration measurements for λ_1 (a), and λ_2(b) modes coupled to the fundamental RBM. Note that when computing the areas the PSD in units of mW/Hz was used.

4. CONVERSION GAIN ESTIMATION

Here we present an experimental estimation of the amplified wavelength conversion gain, $A_{x,\text{exp}}$ using the broadband probe and RSA measurement technique discussed in the main text. In addition to the data shown in Fig. 4(c) of the main text, a measurement of the cavity reflection and OMIT for the λ_2 mode is utilized, as shown in Fig. S4(a). We define the estimated amplification conversion gain, $A_{x,\text{exp}}$, as the ratio of output converted signal power $P_{\text{out}} = \alpha^2_{\lambda_{1,\text{conv}}}$ to the input signal power to be converted, $P_{\text{in}} = \alpha^2_{\lambda_2}\beta^2/4$ where α_{λ_2} is the control field amplitude for the λ_2 mode, and β is the modulation index of the phase modulator driven by the arbitrary waveform generator. Following the methodology described in Section 1 the signal, S_2, or optical power, reflected by the cavity for the OMIT measurement of the λ_2 mode is

$$S_2 = \alpha^2_{\lambda_2}\beta|B|, \quad \textbf{(S20)}$$

where B is defined in Eqn. S13, and $\phi = \pi/2$. We then assume that the off resonant sideband reflection coefficient passes unaffected by the cavity ($r^- = 0$) to write

$$S_2 = \alpha^2_{\lambda_2}\beta|r^+_{\lambda_2}||r^0_{\lambda_2}|, \quad \textbf{(S21)}$$

where the λ_2 subscripts have been added to the reflection coefficients to avoid confusion with the λ_1 mode. For the converted signal, S_1, as measured via the λ_1 mode, we take:

$$r^+_{\text{out}} = 0 \quad \textbf{(S22)}$$
$$r^0_{\text{out}} = r^0\alpha_{\lambda_1}$$
$$r^-_{\text{out}} = \alpha_{\lambda_{1,\text{conv}}}e^{-i(-\omega_m+\omega)t}$$

where α_{λ_1} is the control field amplitude for the λ_1 mode, which results in

$$S_1 = 2|r^0_{\lambda_1}|\alpha_{\lambda_1}\alpha_{\lambda_{1,\text{conv}}}, \quad \textbf{(S23)}$$
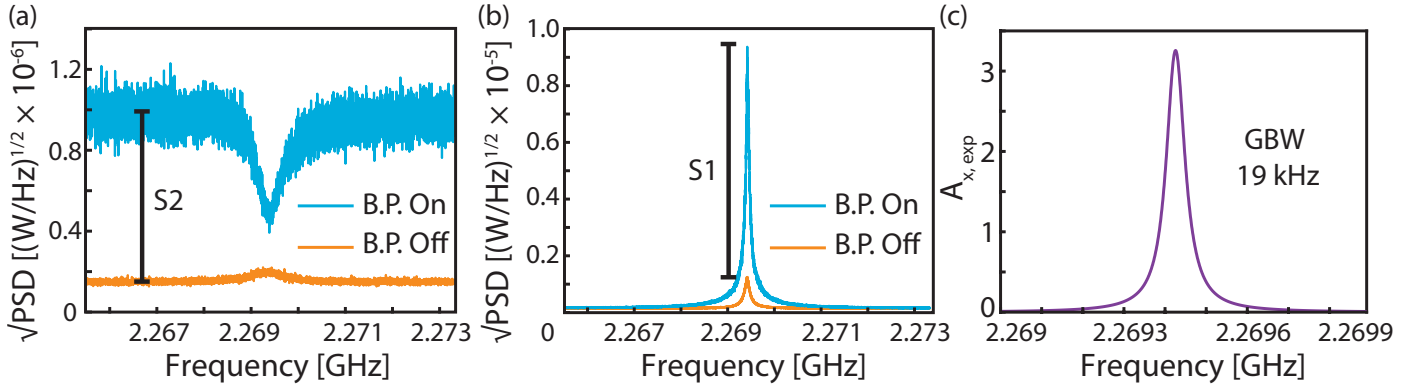
which allows us to write the gain as

Fig. S4. Estimation of amplified wavelength conversion gain, $A_{x, exp}$ utilizing the broadband probe (B.P.) measurement technique. (a) Measurement of cavity reflection and OMIT when the B.P. is on and transduction of the mechanical motion when the B.P. is off, where the λ_1 mode was placed off-resonance for this measurement. We define S_2 as the difference between the maximum of the cavity reflection profile (B.P. on) and the noise floor (B.P. off) which is measured slightly off–resonance to avoid the OMIT feature. (b) Amplified conversion measurement where we define S_2 as the difference between the B.P. on and off measurement to isolate the wavelength converted signal from the thermal component (B.P. off). (c) Conversion gain calculated as a function of frequency where a maximum gain of $A_{x, exp} = 3.2$ is found, resulting in a GBW = 19 kHz.

$$A_{x,exp} = \frac{P_{out}}{P_{in}} = \frac{\alpha_{\lambda_2}^2 |r_{\lambda_2}^0|^2}{\alpha_{\lambda_1}^2 |r_{\lambda_1}^0|^2} \left(\frac{S_1}{S_2}\right)^2 |r_{\lambda_2}^+|^2. \qquad \textbf{(S24)}$$

We can then evaluate Eqn. S24 based on the power we measure at the output of the cavity, the signals we measure on the RSA which are proportional to S_1^2 and S_2^2, and the reflection coefficient for the upper sideband input to the λ_2 mode, $r_{\lambda_2}^+$. To evaluate Eqn. S24 we start by taking advantage of the fact that $\kappa \gg \gamma_m$ such that $r_{\lambda_2}^+$ is flat in the narrow spectral domain about the OMIT feature and set $r_{\lambda_2}^+ = \kappa_e/\kappa$, where we are approximating the on–resonance cavity reflection by measuring S_2 as shown in Fig. S4(a). As the probe is derived from the λ_2 control field we are forced to measure the cavity reflection slightly detuned to avoid the OMIT feature in Fig. S4(a); this measurement is valid up to a constant which characterizes the electronic response of the photodetector. By assuming that the response of the photodetector is similar at both λ_1 and λ_2 this will be normalized out when computing $A_{x,exp}$. We define S_1 as the difference in the measured amplified signal with the broadband probe (B.P.) on and off as shown in Fig. S4(b), which again ignores the photodetector response. The optical power measured at the output of the cavity for each mode is $\alpha_{\lambda_1}^2 |r_{\lambda_1}^0|^2 = 16.0$ mW and $\alpha_{\lambda_2}^2 |r_{\lambda_2}^0|^2 = 3.8$ mW. The signals in Fig. S4(b) were each fit to a Lorentzian which were then used to calculate $A_{x, exp}$ as a function of frequency, as shown in Fig. S4(c). This gives a maximum gain of $A_{x,exp} = 3.2$, and bandwidth of 5.8 kHz, resulting in a gain bandwidth product, GBW = 19 kHz.

REFERENCES

1. C. Bond, D. Brown, A. Freise, and K. A. Strain, "Interferometer techniques for gravitational-wave detection," Living Reviews in Relativity **19**, 3 (2017).
2. L.-S. Yan, Q. Yu, A. E. Willner, and Y. Shi, "Measurement of the chirp parameter of electro-optic modulators by comparison of the phase between two sidebands," Opt. Lett. **28**, 1114–1116 (2003).
3. M. Borselli, T. J. Johnson, and O. Painter, "Beyond the Rayleigh scattering limit in high-Q silicon microdisks: theory and experiment," Opt. Express **13**, 1515–1530 (2005).
4. M. Gorodetksy, A. Schliesser, G. Anetsberger, S. Deleglise, and T. Kippenberg, "Determination of the vacuum optomechanical coupling rate using frequency noise calibration," Opt. Express **18**, 23236–23246 (2010).
5. K. C. Balram, M. I. Davanço, J. D. Song, and K. Srinivasan, "Coherent coupling between radiofrequency, optical and acoustic waves in piezo-optomechanical circuits," Nat. Photon. **10**, 346–352 (2016).
6. K. Schneider and P. Seidler, "Strong optomechanical coupling in a slotted photonic crystal nanobeam cavity with an ultrahigh quality factor-to-mode volume ratio," Opt. Express **24**, 13850–13865 (2016).